

Atomic self-ordering with competing long-range interactions

Stefan Ostermann,^{1,*} Valentin Walther,^{1,2} and Susanne F. Yelin¹

¹*Department of Physics, Harvard University, Cambridge, Massachusetts 02138, USA*

²*ITAMP, Harvard-Smithsonian Center for Astrophysics, Cambridge, Massachusetts 02138, USA*

We study a quantum many-body system with two competing and substantially different long-range interaction potentials. To this end, we consider a two-dimensional BEC in the Rydberg-dressing regime coupled to an optical standing wave resonator. The competition between the two involved interaction potentials, i. e., repulsive soft-core interactions arising due to Rydberg dressing and infinite-range sign changing interactions induced by the cavity photons, allows to control the dynamical pattern formation via collective roton mode softening. In particular, we identify an amorphous solid phase, which can be attributed to geometrical frustration due to competition between the two interaction energies and length scales.

I. INTRODUCTION

The controllability of individual atomic systems increased tremendously over the past decades [1–6]. This enables efficient trapping and cooling of atomic gases or individual atoms, controlling individual photons and tailoring interactions between atoms and photons. One particularly challenging and active modern research direction in this realm are systems with tailored long-range interactions [7]. Prominent examples are, among others, dipolar Bose-Einstein condensates (BECs) [8–11], ultracold atomic gases in cavities [12–14] and individually trapped atoms with Rydberg interactions [15–17]. These systems allow for the study of artificial quantum matter in a well-controlled and tunable environment. They establish a path towards a deeper understanding of interacting quantum many-body systems, which ultimately fosters potential future applications in modern quantum technologies.

A key ingredient for a number of fascinating quantum many-body effects (e.g., supersolidity of dipolar BECs [18–23], feedback induced pattern formation [24–26], etc.) is the competition of various interactions. In this work, we elucidate some of the archetypal effects of such a contest at the example of a particularly clean and experimentally well controlled system: a Rydberg-dressed BEC of neutral atoms trapped in an optical standing wave resonator, see Fig. 1(a). Previous work that combined Rydberg atoms and cavities focused on either generating large optical nonlinearities for single photons [27–29] or spin models on a lattice where the motional degrees of freedom are frozen [29–31]. Here, we focus on the spatial dynamics and resulting density self-ordering of the gas under competing long- and infinite-range interactions. Both constituents considered in this work exhibit a self-ordering phase transition due to roton mode softening [32, 33]. These soft roton modes are a direct result of the respective long-range interactions. However, the two types of interactions have

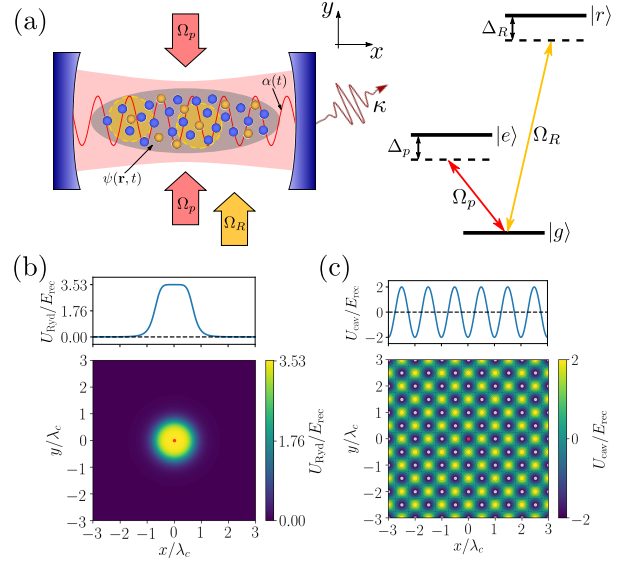


Figure 1. (a) Considered setup. A Rydberg-dressed BEC is trapped and confined to two dimensions in an optical resonator with lasers impinging from the side. The BEC atoms form an effective V-level structure. The transition $|g\rangle \leftrightarrow |e\rangle$ is coupled to the cavity at a strength \mathcal{G}_p . The transition $|g\rangle \leftrightarrow |r\rangle$ is driven by an additional laser in the Rydberg dressing regime, implying that the high-lying Rydberg state $|r\rangle$ is only very weakly populated. The Rydberg dressing imposes a long-range soft-core interaction potential between the atoms, see panel (b). In addition, the cavity photons induce non-trivial infinite range interactions between atoms, see panel (c). The top curves in panels (b) and (c) show cuts along the x -axis at $y = 0.0\lambda_c$ for the two interaction potentials.

substantially different properties. The Rydberg dressing results in spherically symmetric long-range soft-core interactions [see Fig. 1(b)] and the cavity photons induce anisotropic infinite-range periodic interactions between atoms [see Fig. 1(c)]. This distinguishes our work from related studies focusing on a spherically symmetric interaction potential imposing two different length scales [34–36]. In fact, while these works use a synthetic theoretically motivated long-range interaction potential, our study is based on an experimentally realistic configu-

* stefanostermann@g.harvard.edu

ration leading to the non-trivial physics presented below. As we will show in the following, the competition between the two non-trivial interactions at different length scales and the nonlinear interaction between the cavity mode and the BEC leads to the dynamic formation of intriguing phases of quantum matter. In particular, we report the formation of an amorphous solid, which is formed because of geometrical frustration induced by the two competing interaction length scales and energies.

II. MODEL

We consider a pancake-shaped BEC of N atoms confined in two dimensions and trapped inside an optical standing-wave resonator, see Fig. 1(a). The BEC atoms' ground state $|g\rangle$ is coupled via the cavity to a low-lying excited state $|e\rangle$ and, simultaneously, to a highly excited Rydberg s -state $|r\rangle$, realizing the V-configuration illustrated in Fig. 1(a). The BEC atoms are pumped with a laser of frequency ω_p impinging from the side, transverse to the cavity axis, which drives the transition $|g\rangle \leftrightarrow |e\rangle$ at a Rabi frequency Ω_p . This transition couples to a single cavity mode with a coupling strength \mathcal{G}_p . We consider the dispersive regime implying that the detuning $\Delta_p = \omega_p - \omega_{ge}$ is large compared to the Rabi frequency Ω_p (ω_{ge} is the transition frequency between $|g\rangle$ and $|e\rangle$). The transition $|g\rangle \leftrightarrow |r\rangle$ is driven by an additional laser (with frequency ω_R) at a Rabi frequency Ω_R in the Rydberg dressing regime implying a large detuning $\Delta_R \gg \Omega_R$ with $\Delta_R := \omega_R - \omega_{gr}$ (ω_{gr} is the transition frequency between $|g\rangle$ and $|r\rangle$). This allows the adiabatic elimination of the Rydberg state $|r\rangle$ resulting in an effective long-range two-body interaction potential [37–41]

$$U_{\text{Ryd}}(\mathbf{r} - \mathbf{r}') = \frac{\tilde{C}_6}{R_c^6 + |\mathbf{r} - \mathbf{r}'|^6}, \quad (1)$$

which arises due to the strong Van der Waals (VdW) interactions $\propto C_6/|\mathbf{r}|^6$ ($\mathbf{r} \in \mathbb{R}^2$) between Rydberg atoms. The parameters in Eq. (1) are defined as $\tilde{C}_6 := \left(\frac{\Omega_R}{2\Delta_R}\right)^4 C_6$ and $R_c := \left(-\frac{C_6}{2\hbar\Delta_R}\right)^{1/6}$. An exemplary plot of the functional dependence of this long-range interaction potential is shown in Fig. 1(b). It was shown in previous work that a mean-field treatment suffices to capture the main features of cavity self-ordering [12, 13, 42] and Rydberg crystallization induced by the long-range interaction potential given in Eq. (1) [32, 39, 43]. Therefore, we focus on a mean-field treatment. Here, we present the most important equations used throughout this work. A more detailed discussion of the model can be found in Appendix A. The dynamics is governed by two coupled equations. The equation for the BEC order parameter

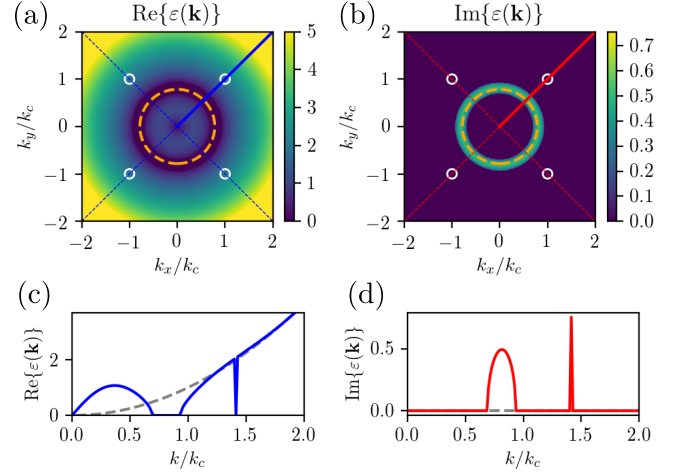


Figure 2. Real and imaginary part of the excitation spectrum given in Eq. (5) for $\tilde{C}_6 = 2.2E_{\text{rec}}$ and $\eta = 1.1\eta_{\text{crit}}$, i.e., both interaction strengths above the threshold condition. The dashed orange circle in panels (a) and (b) marks the roton minimum induced by the spherically symmetric Rydberg interaction. The white circles indicate the four δ -like rotons generated by the cavity interaction potential. Panels (c) and (d) show a cut along the diagonals for positive k_x and k_y values [red and blue lines in panels (a) and (b)]. The other parameters are: $R_c = 0.92\lambda_c$, $\Delta_c = -10.0\omega_{\text{rec}}$, $\kappa = 5.0\omega_{\text{rec}}$ and $U_0 = -1.0\omega_{\text{rec}}$.

$\psi(\mathbf{r}, t)$ is given as

$$\begin{aligned} i\hbar\partial_t\psi(\mathbf{r}, t) = & \left[-\frac{\hbar^2\nabla^2}{2m} \right. \\ & + \hbar U_0|\alpha(t)|^2 \cos^2(k_c x) + 2\hbar\eta\text{Re}[\alpha(t)] \cos(k_c x) \cos(k_c y) \\ & \left. + \int_V d\mathbf{r}' U_{\text{Ryd}}(\mathbf{r} - \mathbf{r}') |\psi(\mathbf{r}', t)|^2 \right] \psi(\mathbf{r}, t), \end{aligned} \quad (2a)$$

and the dynamics of the mean-field cavity mode amplitude $\alpha(t)$ is governed by

$$i\partial_t\alpha(t) = [-\Delta_c + U_0B[\psi] - i\kappa] \alpha(t) + \eta\theta[\psi]. \quad (2b)$$

In Eq. (2b) we introduced the cavity bunching parameter $B[\psi] := \int_V d\mathbf{r} |\psi(\mathbf{r}, t)|^2 \cos^2(k_c x)$ and the cavity mode order parameter $\theta[\psi] := \int_V d\mathbf{r} |\psi(\mathbf{r}, t)|^2 \cos(k_c x) \cos(k_c y)$. The latter is the crucial quantity for understanding the self-ordering phase transition since the cavity mode can only take non-zero values if $\theta[\psi] \neq 0$, whereas the former only accounts for a cavity resonance frequency shift due to the BEC density. The potential depth of the cavity potential generated by inter-cavity photon scattering is defined as $U_0 := \mathcal{G}_p^2/\Delta_p$, and the effective pump strength is $\eta := \Omega_p\mathcal{G}_p/\Delta_p$ in Eq. (2a). In addition, $k_c = 2\pi/\lambda_c$ denotes the cavity wavenumber where λ_c is the cavity resonance wavelength. We also introduced the detuning of the pump laser frequency ω_p with respect to the cavity resonance frequency ω_c as $\Delta_c := \omega_p - \omega_c$ and the cavity decay rate κ .

A particularly simple and insightful model can be obtained in the low-energy regime by adiabatically eliminating the cavity mode (for details, cf. Appendix A), which results in a new effective equation for the BEC dynamics

$$i\hbar\partial_t\psi(\mathbf{r},t) = \left[-\frac{\hbar^2}{2m}\nabla^2 + \int_V d\mathbf{r}' [U_{\text{cav}}(\mathbf{r}-\mathbf{r}') + U_{\text{Ryd}}(\mathbf{r}-\mathbf{r}')] |\psi(\mathbf{r}',t)|^2 \right] \psi(\mathbf{r},t). \quad (3)$$

In Eq. (3) we introduced the cavity two-body interaction potential induced by the cavity photons as

$$U_{\text{cav}}(\mathbf{r}-\mathbf{r}') = \hbar\mathcal{I} \cos[k_c(x-x')] \cos[k_c(y-y')], \quad (4)$$

where $\mathcal{I} := \eta^2(\Delta_c - NU_0/2)/[(\Delta_c - NU_0/2)^2 + \kappa^2]$ is the effective interaction strength. An exemplary plot of this infinite-range interaction potential is shown in Fig. 1(d). It is the competition between the two significantly different types of long-range interaction potentials U_{Ryd} and U_{cav} shown in Figs. 1(b) and (c), which contributes to the non-trivial emergent phases presented below. Note, that the simplified model given in Eq. (3) provides a good intuitive picture about the fundamental interactions induced by the two model constituents. However, this approximate model does not cover all features arising from the nonlinear coupled dynamics of the cavity mode and the BEC [see Eq. (2)], as discussed below.

III. ROTON INSTABILITIES

Roton-induced instabilities were first introduced and studied for superfluid Helium-4 [44] but they are a common feature of systems with long-range interactions. A dynamical instability of a certain nonzero k -mode in the collective excitation spectrum usually results in a phase transitions from homogeneous to periodic order. The Bogoliubov excitation spectrum for plane-wave excitations on top of a homogeneous condensate for a system with two-body long-range interaction potentials reads [45]

$$\varepsilon(\mathbf{k}) = \sqrt{\frac{\hbar^2\mathbf{k}^2}{2m} \left\{ \frac{\hbar^2\mathbf{k}^2}{2m} + 2\rho [U_{\text{Ryd}}(\mathbf{k}) + U_{\text{cav}}(\mathbf{k})] \right\}}, \quad (5)$$

where $U_{\text{Ryd}}(\mathbf{k})$ and $U_{\text{cav}}(\mathbf{k})$ denote the Fourier Transforms (FTs) of the respective interaction potentials $U_{\text{Ryd}}(\mathbf{r}-\mathbf{r}')$ and $U_{\text{cav}}(\mathbf{r}-\mathbf{r}')$. We also introduced the particle density $\rho := N/V$ with V being the total volume of the BEC. The FT of the Rydberg interaction potential cannot be expressed in a comprehensive analytical formula. The FT of the cavity interaction potential (4), however, is given as $U_{\text{cav}}(\mathbf{k}) = \hbar\mathcal{I} \sum_{i,j \in \{0,1\}} \delta_{k_x,(-1)^i k_c} \delta_{k_y,(-1)^j k_c}$, where δ_{k_1,k_2} denotes the Kronecker-delta. In Fig. 2 an exemplary excitation spectrum is shown. The spherically symmetric Rydberg

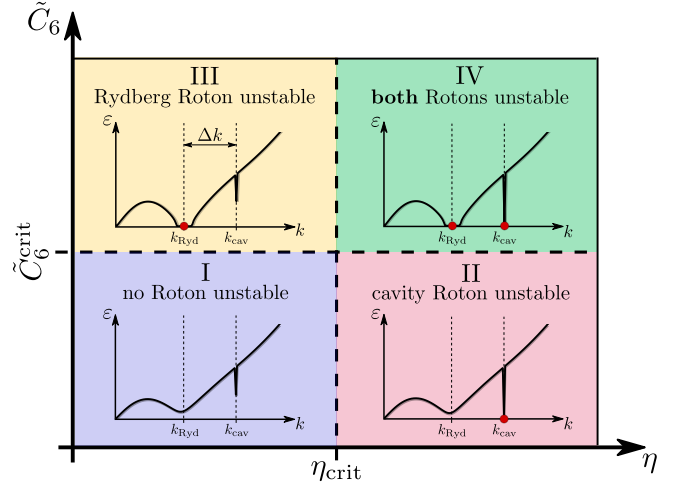


Figure 3. Sketch of the expected phase diagram based on the excitation spectrum. We distinguish four regions: I – no roton softened, i.e., the homogeneous solution is stable, II – the cavity roton touches zero (indicated by red circle), i.e., acquires an imaginary part, III – the Rydberg roton is unstable at $k = k_{\text{Ryd}}$ and IV – both rotors are unstable. The distance Δk between the two k -values at which the rotors soften can be tuned by tuning R_c in Eq. (1).

interaction potential induces roton softening along a circle with a radius k_{Ryd} [indicated by the dashed orange line in Fig. 2(a) and (b)]. The cavity interaction potential, however, results in four δ -shaped peaks/minima which are indicated by the white circles in Fig. 2(a) and (b), and are more prominently visible in panels Fig. 2(c) and (d). Hence, while the two interaction potentials considered in this work both result in dynamical instabilities induced by roton mode softening, the properties of the related excitation spectra differ significantly. The cavity roton positions are always fixed by the cavity wavelength and are located at a value $k_{\text{cav}} := \sqrt{2}k_c$ while the value of k_{Ryd} can be tuned via the parameter R_c in Eq. (1). Since each unstable k -mode can be associated with a characteristic length scale via $k_{\text{Ryd}} = 2\pi/l_{\text{Ryd}}$ and $k_{\text{cav}} = 2\pi/l_{\text{cav}}$, the role of different emergent length scales on the final steady or ground state can be analyzed by changing R_c correspondingly. This can either be achieved by dressing to a different Rydberg state (\tilde{C}_6 scales like n^{11} , where n is the principal quantum number) or by changing the detuning Δ_R .

The homogeneous solution gets unstable toward a periodically ordered pattern if the excitation spectrum acquires an imaginary part at a non-zero \mathbf{k} -value, i.e., $\min[\text{Re}(\varepsilon(\mathbf{k}))|_{|\mathbf{k}|>0}] = 0$. This results in two critical values $\tilde{C}_6^{\text{crit}}$ (critical Rydberg interaction strength) and η_{crit} (critical effective cavity pump strength). Since the FT of the cavity interaction potential is solely given as the sum of four Kronecker-delta functions it is possible to find an analytical expression for the threshold for the pure cavity self-ordering case. Setting \tilde{C}_6 to zero and applying the

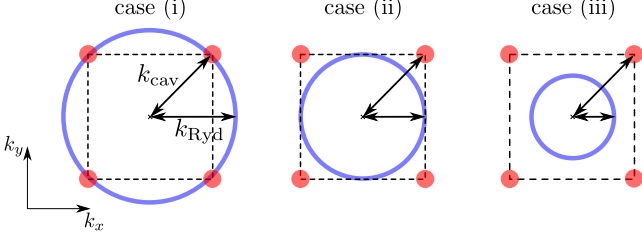


Figure 4. The three cases considered in this work. The red dots mark the four k -modes which are unstable due to the cavity interaction potential (see Fig. 2). The blue circle indicates all k -values which are unstable due to the Rydberg dressing potential. case (i): $k_{\text{Ryd}} = k_{\text{cav}}$, case (ii): $k_{\text{Ryd}} = k_{\text{cav}}/\sqrt{2} = k_c$ and case (iii): $k_{\text{Ryd}} = k_{\text{cav}}/2$. The cases (i) and (ii) represent special cases, whereas case (iii) corresponds to one example for the most general scenario.

threshold condition for $k = k_{\text{cav}}$ in Eq. (5) results in

$$\eta_{\text{crit}} = \sqrt{\frac{(\Delta_c - NU_0/2)^2 + \kappa^2}{NU_0 - 2\Delta_c}} 2\sqrt{\omega_{\text{rec}}}, \quad (6)$$

which is the known threshold for self-organization of a BEC in a cavity in 2D [13].

These insights yield a first intuitive phase diagram shown in Fig. 3. We expect the phase diagram to exhibit four different regions. In each region either no, one or two of the respective rotons are unstable (indicated by red circles in Fig. 3). In addition to the two interaction strengths tuned in the phase diagram, the system features another relevant free parameter – the Rydberg interaction range R_c . In the following we will restrict ourselves to three cases: (i) $k_{\text{Ryd}} = k_{\text{cav}}$ which is obtained by choosing $R_c = 0.51\lambda_c$, (ii) $k_{\text{Ryd}} = k_{\text{cav}}/\sqrt{2} = k_c$ with $R_c = 0.72\lambda_c$ and (iii) $k_{\text{Ryd}} = k_{\text{cav}}/2$ with $R_c = 1.2\lambda_c$. A sketch of the unstable roton length scales in k -space for all three cases is shown in Fig. 4. We restrict ourselves to cases where $k_{\text{Ryd}} < k_{\text{cav}}$ because only in this case the additional Rydberg length scale competes with the length scale set by the cavity potential (see also Appendix B). Note that the first two cases (i) and (ii) are special cases because the two wavenumbers are either the same [case (i)] or k_{Ryd} is commensurate with k_c , i. e., the fundamental length scale along the cavity axis [case (ii)]. Case (iii), however, corresponds to one example of the most general incommensurate scenario. We chose a factor two for the wavenumber ratio in case (iii) but the same qualitative results as presented below were obtained for a variety of different wavenumber ratios.

IV. SELF-CONSISTENT GROUND STATE

One major element of the studied system is the interplay between the dynamic cavity field and the BEC dynamics. While the simplified model given in Eq. (3) provides a good intuitive picture about the features and roles

of the two different interactions, it does not fully capture the competing time scales in the system. Hence, we now analyze the full system given in Eq. (2). We calculate the self-consistent ground state for the set of Eqs. (2) via a variational approach. To this end, we employ a self-consistent iterative algorithm: 1) choose a random initial steady-state value α_{ss} . 2) plug this value into the GPE equation (2a) and perform an imaginary time evolution ($t \rightarrow -i\tau$) to find the lowest energy state. 3) calculate a new steady-state of Eq. (2b) by setting $\partial_t \alpha(t) = 0$ and solving for α . We iterate until we find a state where $|\alpha_{ss}|$ lies within a convergence radius of 10^{-6} . Note that this self-consistent algorithm is not necessarily convex. In general, the energy functional

$$\begin{aligned} \mathcal{E}[\psi] = \int_V d\mathbf{r} & \left[-\frac{\hbar^2 \nabla^2}{2m} + \hbar U_0 |\alpha(t)|^2 \cos^2(k_c x) \right. \\ & + 2\hbar \eta \text{Re}[\alpha(t)] \cos(k_c x) \cos(k_c y) \\ & \left. + \int_V d\mathbf{r}' U_{\text{Ryd}}(\mathbf{r} - \mathbf{r}') |\psi(\mathbf{r}')|^2 \right] |\psi(\mathbf{r})|^2, \quad (7) \end{aligned}$$

which results in the GPE in Eq. (2a), can have multiple local minima for a given value of α . Whether one finds the global minimum or not depends on the initial condition for the imaginary time evolution. Therefore, we perform this algorithm for various different initial conditions and compare the obtained values of $|\alpha|$ and the corresponding ground state energies by evaluating the energy functional in Eq. (7). Only if all initial conditions result in the same energy and mode amplitude the energy minimization problem is convex. For details we refer to Appendix B.

A. Case (i) — equal length scales

We first consider the special case where $k_{\text{Ryd}} = k_{\text{cav}}$ (see Fig. 4), which implies equal length scales $l_{\text{Ryd}} = l_{\text{cav}}$ ($R_c = 0.51\lambda_c$). In this case, the regions II and IV in the phenomenological phase diagram in Fig. 3 are expected to merge. This is verified by the numerical phase diagram shown in Fig. 5(a). It exhibits three different phases a homogeneous phase (HOM), a triangular phase (TRI) [see Fig. 5(b)] and a checkerboard lattice phase (CB) [see Fig. 5(c)]. The TRI state only forms if the Rydberg induced roton is unstable, i. e., beyond the critical Rydberg interaction strength indicated by the red dashed line in Fig. 5(a). For increasing cavity pump, the system organizes in a checkerboard pattern, which is the configuration realized in cavity self-organization without Rydberg dressing [12, 13]. Note, however, that the softening of the Rydberg roton affects the threshold for cavity self-ordering (blue line in Fig. 5(a)). This implies that the effect of the Rydberg roton can be observed already far below the critical Rydberg interaction strength $\tilde{C}_6^{\text{crit}}$. This is a remarkable result as the observation of density modulation due to Rydberg dressing has proven elusive

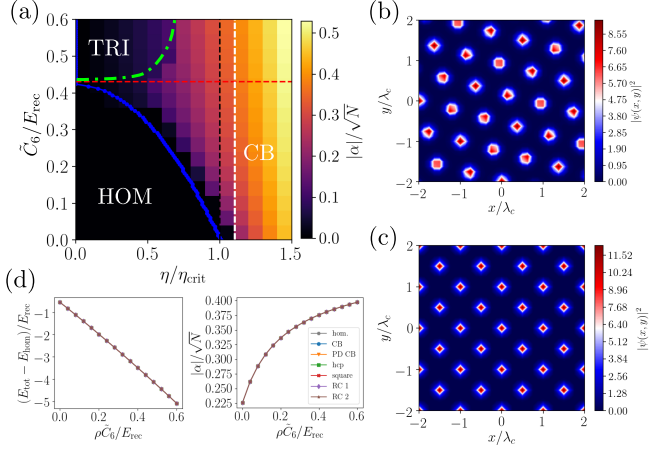


Figure 5. (a) Self-consistent ground state phase diagram for case (i) — $k_{\text{Ryd}} = k_{\text{cav}}$ ($R_c = 0.51\lambda_c$). The dashed black and red curves indicate the critical values for independent Rydberg crystallization (horizontal red dashed) or cavity self-organization (vertical black dashed). The blue curve is the critical value at which the excitation spectrum in Eq. (5) touches zero for the given parameters. The green dash-dotted curve is a guide to the eye indicating the phase boundary. (b) $|\alpha|$ values and ground-state energies (shifted by the energy of the homogeneous solution E_{hom}) for values along the white dashed line in panel (a) for all seven initial conditions. (c) Exemplary density distribution for the triangular (TRI) lattice phase with $\eta = 0.2\eta_{\text{crit}}$ and $\tilde{C}_6 = 0.6E_{\text{rec}}$. (d) Exemplary density distribution for the checkerboard (CB) lattice phase with $\eta = 1.1\eta_{\text{crit}}$ and $\tilde{C}_6 = 0.6E_{\text{rec}}$. All other parameters as in Fig. 2.

in experiments [41] due to experimental complications such as unfavorable scaling with the density and long time scales required for experiments. Our results suggest a way to observe effects of Rydberg dressing indirectly for much smaller Rydberg fractions (i.e., smaller \tilde{C}_6). In Fig. 5(d) we show the obtained ground state energy obtained from Eq. (7) and the cavity mode amplitude for all seven employed initial conditions. We shifted all energies with respect to the homogeneous state energy E_{hom} which is obtained by evaluating Eq. (7) for $\alpha = 0.0$ and a homogeneous BEC density. Energies are given in units of the recoil energy $E_{\text{rec}} := \hbar^2 k_c^2 / (2m) = \hbar\omega_{\text{rec}}$ throughout this work. We find that all curves for all initial conditions lie on top of each other, implying that this particular iterative energy minimization for case (i) is convex in ψ and α .

B. Cases (ii) and (iii) — different length scales

The main property of the considered system is that two interactions with different functional dependence *and* different intrinsic length scale are combined. Here, we show that this feature results in highly non-trivial physics which goes beyond what is achievable with only a sin-

gle model constituent. Fig. 6 exhibits the two obtained ground state phase diagrams together with the additional non-trivial density distributions realized in these regimes. Since now two fundamental length scales become unstable the phase diagram resembles the intuitive picture from Fig. 3 and contains four different phase regions. The critical values obtained via Eq. (5) in section III, however, do not coincide with the numerical values. This shows that the simplified model discussed in section III for the adiabatically eliminated cavity dynamics [see Eq. (3)] provides a good first intuition about the contributing interactions and the expected phase diagram, but fails for different competing length scales due to a break down of the adiabatic solution. This is due to the influence of the additional Rydberg length scale on the mode dynamics which is taken into account in the full numerics resulting in the phase diagrams shown in Fig. 6. The instability in this system is actually induced by the combined collective instability of the BEC density *and* the cavity mode amplitude. The fluctuations of the BEC couple to the fluctuations of the cavity mode and vice versa. This results in actual thresholds for the transitions $\text{TRI} \leftrightarrow \text{SQ}$ and $\text{CB} \leftrightarrow \text{SQ}$ in Fig. 6(a) and $\text{TRI} \leftrightarrow \text{RC}$ and $\text{CB} \leftrightarrow \text{RC}$ in Fig. 6(c) that are below the values anticipated by the simplified excitation spectrum in Eq. (5). This again could facilitate the experimental observation of effects induced due to Rydberg induced roton mode softening at smaller Rydberg interaction strengths \tilde{C}_6 .

For case (ii) we find that, in addition to the TRI and CB phases, a square (SQ) lattice phase emerges [cf. Fig. 6(e)]. This phase is a direct result of the non-trivial interplay between the two different interactions at these particular length scales. All seven initial conditions again result in the same ground state energies and mode amplitudes [see Fig. 6(b)]. This feature changes in the incommensurate case (iii) — $k_{\text{Ryd}} = k_{\text{cav}}/2$. We identify an additional rotated chain (RC) phase [see Fig. 6(c) and (f)], where the iterative energy minimization in the self-consistent algorithm is no longer convex. There are two possible realizations of the RC phase. In Fig. 6(f), we show one possible realization. However, the given density pattern rotated by $\pi/2$ is another ground state with the same energy. This can be seen by the two degenerate lowest energy curves in Fig. 6(d) which correspond to the two possible realizations of the RC phase. The two degenerate states maximize the population of the cavity mode [see Fig. 6(d)] while fulfilling the length scale restrictions imposed by the Rydberg interactions, cf. Appendix B for details. Such degeneracy in combination with non-convex features is a prime indicator for geometrical frustration ultimately leading to glassiness. Note that we restricted our analysis on three cases for a concise presentation of the results. It should be mentioned that cases (i) and (ii) are indeed two special cases, which lead to a convex problem. Any other choice (case (iii) is one possibility) of length scale ratios results in a non-convex energy landscape.

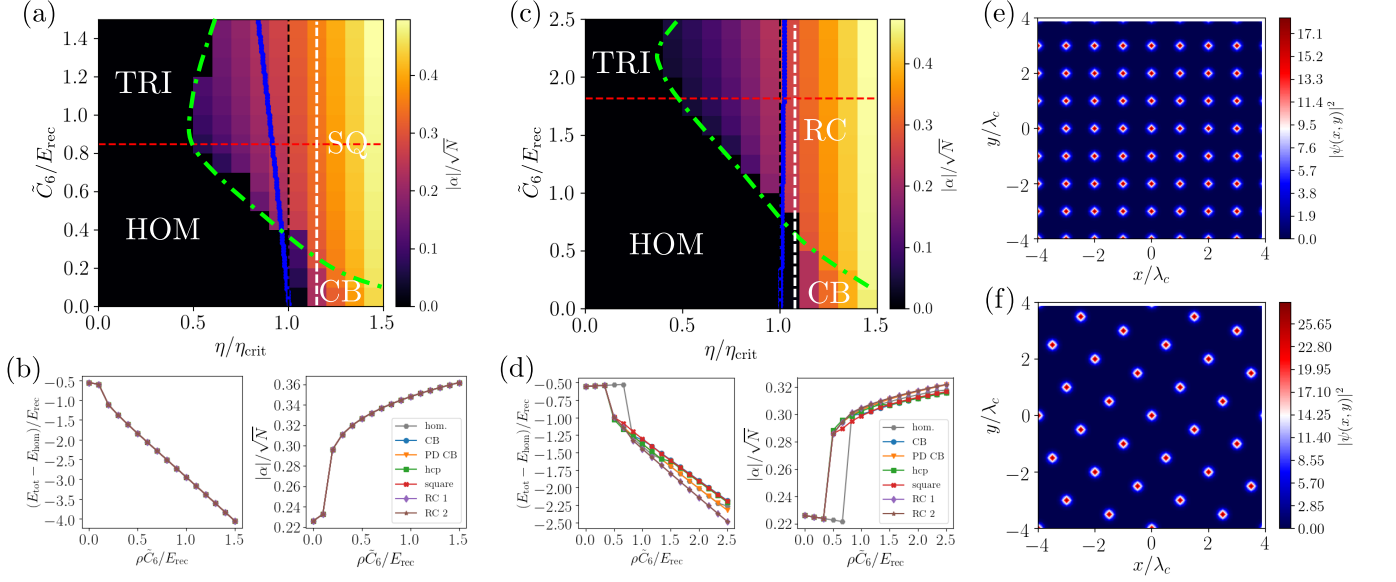


Figure 6. (a) Numerical phase diagram for case (ii) — $k_{\text{Ryd}} = k_{\text{cav}}/\sqrt{2}$ ($R_c = 0.72\lambda_c$). (b) Ground-state energy and cavity mode amplitude $|\alpha|$ along the white vertical dashed line in panel (a) for all seven initial conditions. (c) Numerical phase diagram for case (iii) — $k_{\text{Ryd}} = k_{\text{cav}}/2$ ($R_c = 1.2\lambda_c$). (d) Same as (c) but for case (iii). The different initial conditions no longer result in the same ground-state energies and mode amplitudes. The iterative energy minimization is not convex. (e) Exemplary ground-state density distribution for the square (SQ) phase for case (ii). (f) Exemplary ground state density distribution for the rotated chain phase for case (iii). Note that the same density distribution rotated by $\pi/2$ is a ground state as well, as the degeneracy between RC 1 and RC 2 in panel (d) indicates. The lines on top of the color coding in panels (a) and (c) and all other parameters are the same quantities as in Fig. 5(a).

V. DYNAMICS

It is a priori unclear whether the self-consistent ground state can be reached by dynamically evolving Eq. (2) in real time. While this is usually the case for systems with a unique lowest-energy state, ground-state degeneracy in combination with higher lying energy states may block the dynamical realization of the RC phase in case (iii). In fact, we will show below that the steady-state for case (iii) is an amorphous solid with no long-range density order.

In Fig. 7, the time evolution of the cavity mode amplitude and the total energy together with the steady-state density distribution at $t = 500/\omega_{\text{rec}}$ is shown for case (ii). We find that the square lattice obtained in the previous section is a stable steady state, which can be obtained dynamically when starting from a homogeneous BEC. In contrast, the steady state for case (iii) is stable but *not* the rotated chain state as the self-consistent phase diagram suggests. The steady state is an inhomogeneous density pattern with no long-range density order. In Fig. 8(a), we show three outcomes for three independent runs of the time evolution for the same parameters. Every run results in a different density distribution. This glassy behavior can be directly understood from the nonconvex properties and the degeneracy of the energies found in the previous section [see Fig. 6(f)]. Remarkably, each run results in a different density distribution

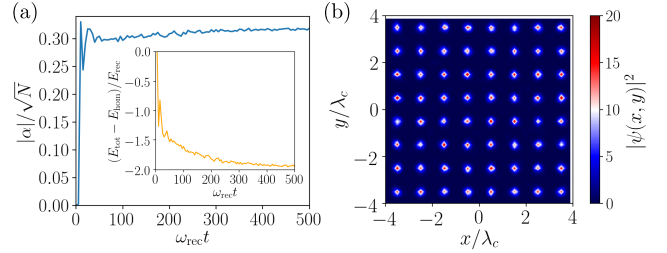


Figure 7. (a) Time evolution of the cavity mode amplitude for case (ii). The inset shows the corresponding time evolution of the total energy obtained via Eq. (7). (b) Steady-state at $t = 500/\omega_{\text{rec}}$. Parameters: $\eta = 1.1\eta_{\text{crit}}$, $\tilde{C}_6 = 1.0E_{\text{rec}}$, $R_c = 0.72\lambda_c$. All other parameters as in Fig. 2.

but exactly the same steady-state cavity mode amplitude. Hence, the different glassy states are not distinguishable via the cavity fields.

VI. CONCLUSIONS AND OUTLOOK

We showed that combining the spherically symmetric long-range interactions induced in a Rydberg-dressed BEC with infinite-range cavity-induced interactions establishes a versatile platform for studying the interplay between different interaction types and landscapes on the phases of quantum matter. The dynamical instability to-

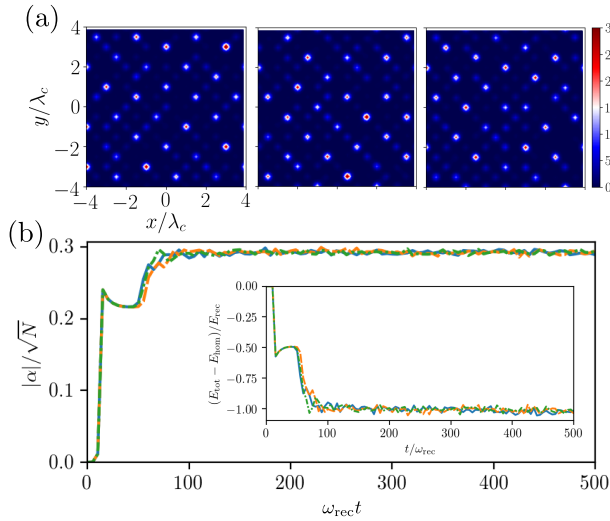


Figure 8. (a) Three different steady-states for three runs for case (iii). Each run generates a different density pattern with no long range order. This is a typical indication of an amorphous solid (or a glassy phase). All realized patterns, however, scatter exactly the same amount of light into the cavity as it can be seen from panel (b). Parameters: $\eta = 1.1\eta_{\text{crit}}$, $\tilde{C}_6 = 1.5E_{\text{rec}}$, $R_c = 1.2\lambda_c$. All other parameters as in Fig. 2.

wards density ordering is induced by the combination of two substantially different forms of roton mode softening. This results in intriguing emergent phases depending on the two length scales fixed by the two unstable roton modes. In particular, the non-convex nature of the energy minimization problem in the incommensurate case (iii) enables a phase transition from a solid (CB phase) to an amorphous solid by tuning the Rydberg interaction strength. Despite the fact that each dynamical realization exhibits a different density distribution with no long-range order, all realizations result in the same cavity mode population. This exhibits the highly non-linear nature of the underlying processes, since energy minimization involves two entities: the BEC wave function ψ and the cavity mode α . It is the interplay between these two dynamic quantities which gives rise to the intriguing effects presented here. The related finding that the coupling between density fluctuations and the cavity mode facilitates the softening of the Rydberg roton might open an avenue to observe effects of the Rydberg induced instabilities experimentally. Our findings also have potential applications in modern quantum technologies: The formation of a density ordered pattern in this hybrid system ultimately resembles a quantum optimization problem. Hence, the system could be tailored to particular optimization problems. In addition, glassy states are promising candidates for efficient quantum memories.

Our work lays the ground for a variety of further studies combining long-range interacting systems theoretically as well as experimentally. This research avenue is fostered by the new experimental and theoretical opportunities opening up in recently established experimental

setups all over the world. Our proposed setup should be realizable in state-of-the-art cavity QED setups. In particular, the realization of the glassy phase where the parameters are favorable for experiments could readily be realized. However, the setup presented here is not the only system which is expected to exhibit such intriguing properties. Other promising avenues are combining other systems exhibiting light-induced instabilities in free space [24–26, 46–49] with Rydberg dressing or long-range dipole interactions. More control over a wide range of realizable density patterns is expected if one assumes even more complex cavity-induced interaction potentials or Rydberg interactions. This can be achieved by changing to more complex cavity geometries such as multi-mode resonators [50–52] or dressing to spherically asymmetric Rydberg p -states [53, 54]. From a quantum optical viewpoint the dynamic transverse coupling of Rydberg atoms to a cavity could result in a highly nonlinear mechanism to enhance the achievable nonlinearities with state-of-the-art setups.

While this work focused on highlighting the remarkable features of this system and their intriguing consequences, several directions remain open for further research. One open and exciting question is the connection of the formation of the glassy phase to Anderson localization or even many-body localization. Also, the role of beyond mean-field effects and temperature needs further investigation. To answer these questions, alternative theoretical techniques, which go beyond the scope of the present manuscript, have to be developed and applied [55–58]. In any case, the results presented in this work open up exciting avenues in the growing research field of hybrid quantum systems with long-range interactions.

ACKNOWLEDGMENTS

We would like to thank Helmut Ritsch for fruitful discussions. S.F.Y. would like to acknowledge funding by the AFOSR (applications of dense atomic media), the NSF (theory of dense atomic media), and the DOE (structure of 2D atomic media). S.O. is supported by a postdoctoral fellowship of the Max Planck - Harvard Research Center for Quantum Optics (MPHQ). V.W. acknowledges support from the NSF through a grant for the Institute for Theoretical Atomic, Molecular, and Optical Physics at Harvard University and the Smithsonian Astrophysical Observatory.

The numerical simulations were performed with the open-source framework `QuantumOptics.jl` [59].

Appendix A: Detailed model derivation

In the following we provide a concise derivation of the model presented in section II. For a more detailed discussion of the underlying physics we refer to Refs. [60] and [39]. The full many-body Hamiltonian for the con-

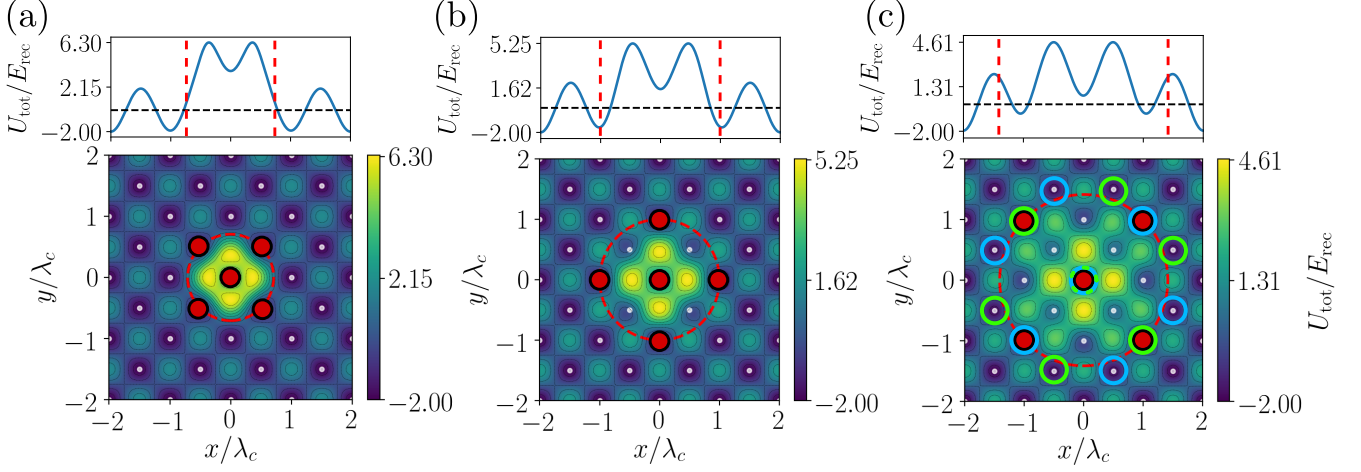


Figure 9. Exemplary total interaction potentials from Eq. (B1) for the three cases treated throughout this work. (a) Case (i); $\eta = 1.0\eta_{\text{crit}}$ and $\tilde{C}_6 = 0.1E_{\text{rec}}$, (b) Case (ii); $\eta = 1.0\eta_{\text{crit}}$ and $\tilde{C}_6 = 0.5E_{\text{rec}}$, (c) Case (iii); $\eta = 1.0\eta_{\text{crit}}$ and $\tilde{C}_6 = 3.0E_{\text{rec}}$. The red dashed lines indicate the length scale imposed by the Rydberg roton. In panels (a) and (b) the red dots mark the first potential minima fulfilling the length scale restrictions imposed via the soft-core interaction potential. In panel (c) the light green and blue circles mark additional configurations fulfilling this restriction. This gives rise to a larger number of potential self-consistent ground states ultimately leading to the glassy behavior discussed in the main text. The dashed red lines indicate the length scale imposed by the Rydberg interaction potential for the respective cases.

sidered system can be written as the sum of five Hamiltonians $H = H_a + H_{a-c} + H_c + H_{\text{int}}^{2-\text{b.}} + H_{\text{int}}^{\text{Ryd}}$ with

$$H_a = \int d\mathbf{r} \Psi^\dagger(\mathbf{r}) \left[-\frac{\hbar^2 \nabla^2}{2m} + \hbar U_p \cos^2(k_c y) \right] \Psi(\mathbf{r}), \quad (\text{A1a})$$

$$H_{a-c} = \int d\mathbf{r} \Psi^\dagger(\mathbf{r}) [\hbar U_0 \cos^2(k_c x) a^\dagger a + \hbar \eta \cos(k_c x) \cos(k_c y) (a + a^\dagger)] \Psi(\mathbf{r}), \quad (\text{A1b})$$

$$H_c = -\hbar \Delta_c a^\dagger a, \quad (\text{A1c})$$

$$H_{\text{int}}^{2-\text{b.}} = \frac{g}{2} \int d\mathbf{r} \Psi^\dagger(\mathbf{r}) \Psi^\dagger(\mathbf{r}) \Psi(\mathbf{r}) \Psi(\mathbf{r}) \quad (\text{A1d})$$

$$H_{\text{int}}^{\text{Ryd}} = \iint d\mathbf{r} d\mathbf{r}' \Psi^\dagger(\mathbf{r}) \Psi^\dagger(\mathbf{r}') \frac{\tilde{C}_6}{R_c^6 + |\mathbf{r} - \mathbf{r}'|^6} \Psi(\mathbf{r}') \Psi(\mathbf{r}). \quad (\text{A1e})$$

Here, Ψ (Ψ^\dagger) are annihilation (creation) operators of bosonic ground state atoms, i.e., $[\Psi(\mathbf{r}), \Psi^\dagger(\mathbf{r}')] = \delta(\mathbf{r} - \mathbf{r}')$ and a (a^\dagger) are annihilation (creation) operators of the photonic cavity mode fulfilling $[a, a^\dagger] = 1$. $U_p := \Omega_p^2/\Delta_p$ is the potential depth of the lattice generated by the two interfering pump beams and $U_0 := \mathcal{G}_p^2/\Delta_p$ is the depth of the optical potential generated by photon scattering from the atomic density distribution inside the cavity. The effective cavity pump strength is given as $\eta := \Omega_p \mathcal{G}_p/\Delta_p$ and $k_c = 2\pi/\lambda_c$ denotes the wavenumber of the cavity mode. The Hamiltonian in Eq. (A1d) takes into account local two-body interactions between atoms and is omitted throughout this work. This is a reasonable assumption since this interaction strength can be tuned to be small via, e.g., a Feshbach resonance

such that cavity and Rydberg induced long-range interactions dominate the dynamics [39, 61]. The dynamics of the hybrid atom-cavity system is governed by the Heisenberg-Langevin equations $i\hbar \partial_t \Psi(\mathbf{r}, t) = [\Psi(\mathbf{r}, t), H]$ and $i\hbar \partial_t a(t) = [a(t), H] - i\hbar \kappa a(t)$ where the decay of the cavity mode at a rate κ is included. Calculating these equations of motion and performing a mean-field approximation via $\Psi(\mathbf{r}, t) \rightarrow \langle \Psi(\mathbf{r}, t) \rangle := \psi(\mathbf{r}, t)$ and $a(t) \rightarrow \langle a(t) \rangle := \alpha(t)$, results in the two coupled c-number equations for the BEC order parameter $\psi(\mathbf{r}, t)$ and the cavity mode amplitude $\alpha(t)$ given in Eq. (2) of the main text.

To adiabatically eliminate the cavity mode we calculate the equation of motion for the field operator a and solve for its steady-state ($\partial_t a = 0$). This results in

$$a_{\text{ss}} = \frac{\eta \int d\mathbf{r} \Psi^\dagger(\mathbf{r}, t) \cos(k_c x) \cos(k_c y) \Psi(\mathbf{r}, t)}{[\Delta_c - U_0 \int d\mathbf{r} \Psi^\dagger(\mathbf{r}, t) \cos^2(k_c x) \Psi(\mathbf{r}, t)] + i\kappa}. \quad (\text{A2})$$

Apart from the fundamental cavity parameters η , Δ_c and κ the steady-state value for the cavity mode is determined by the two quantities

$$\Theta[\Psi(\mathbf{r}, t)] := \int d\mathbf{r} \Psi^\dagger(\mathbf{r}, t) \cos(k_c x) \cos(k_c y) \Psi(\mathbf{r}, t), \quad (\text{A3})$$

$$\mathcal{B}[\Psi(\mathbf{r}, t)] := \int d\mathbf{r} \Psi^\dagger(\mathbf{r}, t) \cos^2(k_c x) \Psi(\mathbf{r}, t). \quad (\text{A4})$$

These two quantities obviously depend on the BEC state which exhibits the non-trivial coupling between the cavity mode and the BEC. While \mathcal{B} only acts as an effective shift of the cavity resonance frequency that comes into play as soon as $a_{\text{ss}} \neq 0$, Θ is the crucial parameter when

it comes to understanding the cavity self-ordering phase transition. The cavity mode is nonzero if $\Theta \neq 0$. Hence this parameter is crucial for the instability described in the main text. To simplify the model we replace \mathcal{B} with its value for the homogeneous condensate $\mathcal{B} = N/2$ while keeping the full functional dependence of Θ . To elimi-

nate the cavity field we plug the resultant steady-state solution into the many-body Hamiltonian. Since we are solely interested in a model capturing the dynamic instability which is governed by terms $\propto \cos(k_c x) \cos(k_c y)$ (see argument above) we keep only these terms. This results in the effective interaction Hamiltonian

$$\begin{aligned} H_{\text{int}}^{\text{cav}} &= \hbar \mathcal{I} \iint d\mathbf{r} d\mathbf{r}' \Psi^\dagger(\mathbf{r}) \Psi^\dagger(\mathbf{r}') \cos(k_c x) \cos(k_c x') \cos(k_c y) \cos(k_c y') \Psi(\mathbf{r}') \Psi(\mathbf{r}) \\ &= \hbar \mathcal{I} \iint d\mathbf{r} d\mathbf{r}' \Psi^\dagger(\mathbf{r}) \Psi^\dagger(\mathbf{r}') \cos[k_c(x - x')] \cos[k_c(y - y')] \Psi(\mathbf{r}') \Psi(\mathbf{r}). \end{aligned} \quad (\text{A5})$$

where we used the symmetry of the cosine function in the second line and introduced the cavity induced interaction strength as

$$\mathcal{I} = \frac{\eta^2(\Delta_c - NU_0/2)}{(\Delta_c - NU_0/2)^2 + \kappa^2}. \quad (\text{A6})$$

The many-body Hamiltonian for the BEC then reduces to $\tilde{H} = - \int d\mathbf{r} \Psi^\dagger(\mathbf{r}) \frac{\hbar^2 \nabla^2}{2m} \Psi(\mathbf{r}) + H_{\text{int}}^{\text{cav}} + H_{\text{int}}^{\text{Ryd}}$. The mean-field equation of motion given in Eq. (3) of the main text is found by calculating the Heisenberg equation of motion for $\Psi(\mathbf{r}, t)$ and again performing the mean-field approximation.

Note that in both GPE equations presented in the main text [Eqs. (2a) and (3)] we neglected the potential term $\propto \cos^2(k_c y)$, which arises due to interference of the pump beams [see Eq. (A1a)]. This term is irrelevant for understanding the collective instabilities and the main fundamental results presented in this work also hold if this term is included as we checked by including it in the numerics. However, neglecting this term facilitates the interpretation of the results and provides a method to understand the fundamental physics from an intuitive semi-analytical standpoint as it is outlined in section III of the main text. In fact, the interference between the two pump beams could even be suppressed in real experimental setups. This can either be achieved by choosing a large enough frequency difference between the two pump beams, or by using two counterpropagating beams with orthogonal polarization. In this case, the model in Eq. (2) becomes exact.

Appendix B: Variational algorithm

To find the self-consistent ground state in section IV we employ a variational algorithm. Here we discuss this algorithm in more detail. In particular, we focus on our choice of initial conditions and argue why the chosen initial conditions are good guesses for the final ground states. In Fig. 9, exemplary plots for the total interac-

tion potential

$$U_{\text{tot}}(\mathbf{r} - \mathbf{r}') = U_{\text{cav}}(\mathbf{r} - \mathbf{r}') + U_{\text{Ryd}}(\mathbf{r} - \mathbf{r}'), \quad (\text{B1})$$

defined as the sum of the two individual interaction potentials given in Eq. (1) and (4) are shown. These potentials provide a good intuition about the anticipated ground states. Hence, we use these potentials as a guideline to define the initial conditions for the imaginary time evolution. We see that for the two special cases (i) ($k_{\text{cav}} = k_{\text{Ryd}}$) and (ii) ($k_{\text{cav}} = k_{\text{Ryd}}/\sqrt{2}$), the interaction potentials suggest a checkerboard pattern and a square lattice as a ground state which is indeed the self-consistent ground state in these particular cases [cf. Figs. 5(d) and Fig. 6(e)]. In addition, to those cases we choose the hexagonal closed packed (hcp) lattice as an additional initial condition for all cases because this would be the ground state for a Rydberg-dressed BEC without cavity interactions [32]. From Fig. 9 we see that case (iii) is more complex than the previous two cases. In this case, the ground state could be a checkerboard lattice with larger period than in case (i) [see red dots in Fig. 9(c)] or one of the two lattice configurations indicated by the light green and blue circles in Fig. 9(c). Based on the above arguments it also becomes clear that only the cases where $k_{\text{Ryd}} < k_{\text{cav}}$ results in modified results. If this condition is not fulfilled the length scale imposed by the Rydberg interaction potential is smaller than the cavity interaction potential which only modifies the corresponding interaction potential locally [see Fig. 9(a)].

Based on these intuitive arguments we generate the respective initial states $\psi(\mathbf{r}) = \sum_i \phi_\sigma(\mathbf{r} - \mathbf{R}_i)$ by superimposing Gaussian wave functions $\phi_\sigma(\mathbf{r}) = C \exp[-|\mathbf{r}|^2/(2\sigma^2)]$. The resultant non-trivial initial conditions (we refrain from showing the homogeneous density) are shown in Fig. 10. We run the variational algorithm discussed in section IV for all these initial conditions for all cases (i)-(iii). We then compare the ground-state energies calculated via Eq. (7) and the resultant cavity mode amplitude to estimate whether the respective optimization problem is convex or not.

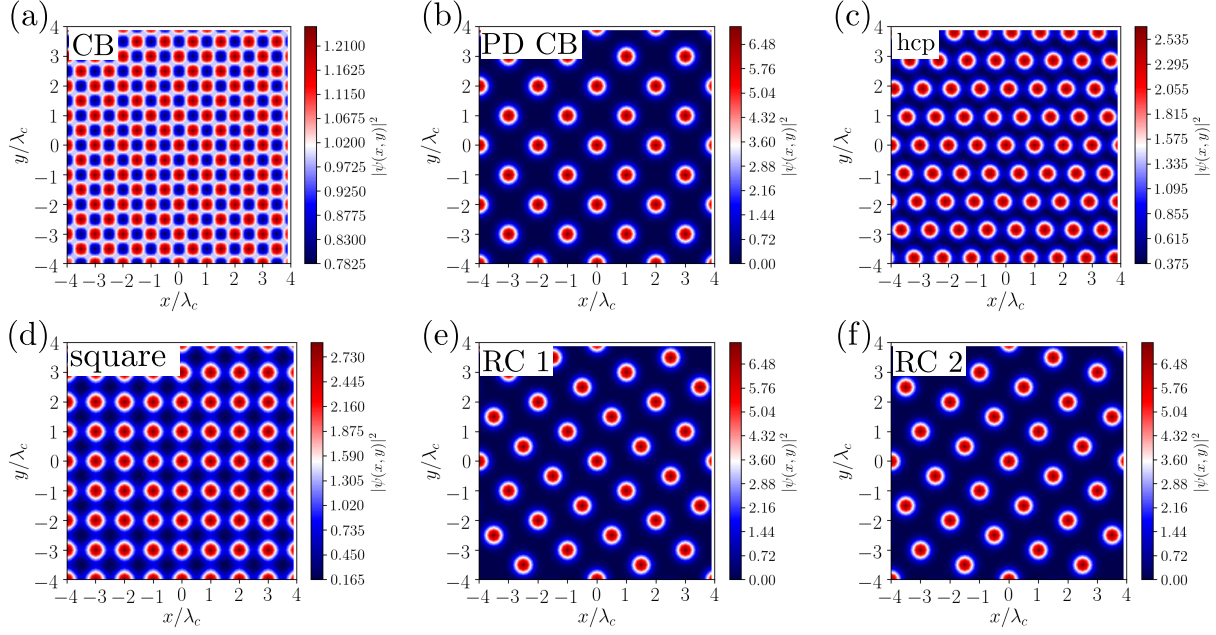


Figure 10. The six non-trivial initial conditions (we refrain from showing the homogeneous state) based on the intuitive picture drawn in Fig. 9. (a) checkerboard pattern (CB), (b) period-doubled checkerboard pattern (PD CB), (c) hexagonal closed pack (hcp), (d) square lattice, (e) rotated chain version 1 (RC 1) and (f) rotated chain version 2 (RC 2).

-
- [1] H. J. Metcalf and P. van der Straten, Laser cooling and trapping of atoms, *J. Opt. Soc. Am. B* **20**, 887 (2003).
 - [2] S. Haroche and J.-M. Raimond, *Exploring the Quantum: Atoms, Cavities, and Photons* (Oxford University Press, 2006).
 - [3] I. Bloch, J. Dalibard, and W. Zwerger, Many-body physics with ultracold gases, *Reviews of Modern Physics* **80** (2008).
 - [4] A. Reiserer and G. Rempe, Cavity-based quantum networks with single atoms and optical photons, *Reviews of Modern Physics* **87** (2015).
 - [5] C. Gross and I. Bloch, Quantum simulations with ultracold atoms in optical lattices, *Science* **357** (2017).
 - [6] A. Browaeys and T. Lahaye, Many-body physics with individually controlled Rydberg atoms, *Nature Physics* **16** (2020).
 - [7] N. Defenu, T. Donner, T. Macrì, G. Pagano, S. Ruffo, and A. Trombettoni, Long-range interacting quantum systems, *arXiv:2109.01063* (2021).
 - [8] A. Griesmaier, J. Werner, S. Hensler, J. Stuhler, and T. Pfau, Bose-Einstein Condensation of Chromium, *Physical Review Letters* **94**, 160401 (2005).
 - [9] M. Lu, N. Q. Burdick, S. H. Youn, and B. L. Lev, Strongly Dipolar Bose-Einstein Condensate of Dysprosium, *Physical Review Letters* **107**, 190401 (2011).
 - [10] K. Aikawa, A. Frisch, M. Mark, S. Baier, A. Rietzler, R. Grimm, and F. Ferlaino, Bose-Einstein Condensation of Erbium, *Physical Review Letters* **108** (2012).
 - [11] M. A. Norcia and F. Ferlaino, New opportunities for interactions and control with ultracold lanthanides, *arXiv:2108.04491* (2021).
 - [12] H. Ritsch, P. Domokos, F. Brennecke, and T. Esslinger, Cold atoms in cavity-generated dynamical optical potentials, *Rev. Mod. Phys.* **85** (2013).
 - [13] F. Mivehvar, F. Piazza, T. Donner, and H. Ritsch, Cavity QED with Quantum Gases: New Paradigms in Many-Body Physics, *arXiv:2102.04473* (2021).
 - [14] A. Periwal, E. S. Cooper, P. Kunkel, J. F. Wienand, E. J. Davis, and M. Schleier-Smith, Programmable Interactions and Emergent Geometry in an Atomic Array, *arXiv:2106.04070* (2021).
 - [15] S. Ebadi, T. T. Wang, H. Levine, A. Keesling, G. Semeghini, A. Omran, D. Bluvstein, R. Samajdar, H. Pichler, W. W. Ho, S. Choi, S. Sachdev, M. Greiner, V. Vuletić, and M. D. Lukin, Quantum phases of matter on a 256-atom programmable quantum simulator, *Nature* **595** (2021).
 - [16] P. Scholl, M. Schuler, H. J. Williams, A. A. Eberharter, D. Barredo, K.-N. Schymik, V. Lienhard, L.-P. Henry, T. C. Lang, T. Lahaye, A. M. Läuchli, and A. Browaeys, Quantum simulation of 2D antiferromagnets with hundreds of Rydberg atoms, *Nature* **595** (2021).
 - [17] G. Semeghini, H. Levine, A. Keesling, S. Ebadi, T. T. Wang, D. Bluvstein, R. Verresen, H. Pichler, M. Kalinowski, R. Samajdar, A. Omran, S. Sachdev, A. Vishwanath, M. Greiner, V. Vuletic, and M. D. Lukin, Probing Topological Spin Liquids on a Programmable Quantum Simulator, *arXiv:2104.04119* (2021).
 - [18] F. Böttcher, J.-N. Schmidt, M. Wenzel, J. Hertkorn, M. Guo, T. Langen, and T. Pfau, Transient Supersolid Properties in an Array of Dipolar Quantum Droplets, *Phys. Rev. X* **9** (2019).

- [19] L. Tanzi, E. Lucioni, F. Famà, J. Catani, A. Fioretti, C. Gabbanini, R. N. Bisset, L. Santos, and G. Modugno, Observation of a Dipolar Quantum Gas with Metastable Supersolid Properties, *Phys. Rev. Lett.* **122** (2019).
- [20] L. Chomaz, D. Petter, P. Ilzhöfer, G. Natale, A. Trautmann, C. Politi, G. Durastante, R. M. W. van Bijnen, A. Patscheider, M. Sohmen, M. J. Mark, and F. Ferlaino, Long-Lived and Transient Supersolid Behaviors in Dipolar Quantum Gases, *Phys. Rev. X* **9** (2019).
- [21] J. Hertkorn, J.-N. Schmidt, M. Guo, F. Böttcher, K. S. H. Ng, S. D. Graham, P. Uerlings, T. Langen, M. Zwierlein, and T. Pfau, Pattern formation in quantum ferrofluids: From supersolids to superglasses, *Physical Review Research* **3** (2021).
- [22] T. Bland, E. Poli, C. Politi, L. Klaus, M. A. Norcia, F. Ferlaino, L. Santos, and R. N. Bisset, Two-dimensional supersolidity in a circular trap, *arXiv:2107.06680* (2021).
- [23] M. A. Norcia, C. Politi, L. Klaus, E. Poli, M. Sohmen, M. J. Mark, R. N. Bisset, L. Santos, and F. Ferlaino, Two-dimensional supersolidity in a dipolar quantum gas, *Nature* **596** (2021).
- [24] Y.-C. Zhang, V. Walther, and T. Pohl, Long-Range Interactions and Symmetry Breaking in Quantum Gases through Optical Feedback, *Phys. Rev. Lett.* **121** (2018).
- [25] Y.-C. Zhang, V. Walther, and T. Pohl, Self-bound droplet clusters in laser-driven Bose-Einstein condensates, *Phys. Rev. A* **103** (2021).
- [26] G. Baio, G. R. Robb, A. M. Yao, G.-L. Oppo, and T. Ackemann, Multiple Self-Organized Phases and Spatial Solitons in Cold Atoms Mediated by Optical Feedback, *Physical Review Letters* **126** (2021).
- [27] A. Grankin, E. Brion, E. Bimbard, R. Boddada, I. Usmani, A. Ourjountsev, and P. Grangier, Quantum-optical nonlinearities induced by Rydberg-Rydberg interactions: A perturbative approach, *Phys. Rev. A* **92** (2015).
- [28] R. Boddada, I. Usmani, E. Bimbard, A. Grankin, A. Ourjountsev, E. Brion, and P. Grangier, Rydberg-induced optical nonlinearities from a cold atomic ensemble trapped inside a cavity, *J. Phys. B – At. Mol. Opt.* **49** (2016).
- [29] J. Gelhausen, M. Buchhold, A. Rosch, and P. Strack, Quantum-optical magnets with competing short- and long-range interactions: Rydberg-dressed spin lattice in an optical cavity, *SciPost Phys.* **1** (2016).
- [30] P. Strack and S. Sachdev, Dicke Quantum Spin Glass of Atoms and Photons, *Phys. Rev. Lett.* **107** (2011).
- [31] S. Gopalakrishnan, B. L. Lev, and P. M. Goldbart, Frustration and Glassiness in Spin Models with Cavity-Mediated Interactions, *Phys. Rev. Lett.* **107** (2011).
- [32] N. Henkel, F. Cinti, P. Jain, G. Pupillo, and T. Pohl, Supersolid Vortex Crystals in Rydberg-Dressed Bose-Einstein Condensates, *Phys. Rev. Lett.* **108** (2012).
- [33] R. Mottl, F. Brennecke, K. Baumann, R. Landig, T. Donner, and T. Esslinger, Roton-Type Mode Softening in a Quantum Gas with Cavity-Mediated Long-Range Interactions, *Science* **336** (2012).
- [34] K. Barkan, M. Engel, and R. Lifshitz, Controlled Self-Assembly of Periodic and Aperiodic Cluster Crystals, *Physical Review Letters* **113** (2014).
- [35] B. R. de Abreu, F. Cinti, and T. Macrì, Superstripes and quasicrystals in bosonic systems with hard-soft corona interactions, *arXiv:2009.10203* (2020).
- [36] G. Pupillo, P. Zitherl, and F. Cinti, Quantum cluster quasicrystals, *Physical Review B* **101** (2020).
- [37] J. E. Johnson and S. L. Rolston, Interactions between Rydberg-dressed atoms, *Phys. Rev. A* **82** (2010).
- [38] J. Honer, H. Weimer, T. Pfau, and H. P. Büchler, Collective Many-Body Interaction in Rydberg Dressed Atoms, *Phys. Rev. Lett.* **105** (2010).
- [39] N. Henkel, R. Nath, and T. Pohl, Three-Dimensional Roton Excitations and Supersolid Formation in Rydberg-Excited Bose-Einstein Condensates, *Phys. Rev. Lett.* **104** (2010).
- [40] F. Maucher, N. Henkel, M. Saffman, W. Królikowski, S. Skupin, and T. Pohl, Rydberg-Induced Solitons: Three-Dimensional Self-Trapping of Matter Waves, *Phys. Rev. Lett.* **106** (2011).
- [41] J. B. Balewski, A. T. Krupp, A. Gaj, S. Hofferberth, R. Löw, and T. Pfau, Rydberg dressing: understanding of collective many-body effects and implications for experiments, *New J. Phys.* **16**, 063012 (2014).
- [42] D. Nagy, G. Szirmai, and P. Domokos, Self-organization of a Bose-Einstein condensate in an optical cavity, *Eur. Phys. J. D* **48** (2008).
- [43] C.-H. Hsueh, T.-C. Lin, T.-L. Horng, and W. C. Wu, Quantum crystals in a trapped Rydberg-dressed Bose-Einstein condensate, *Phys. Rev. A* **86**, 013619 (2012).
- [44] L. Landau, Theory of the Superfluidity of Helium II, *Physical Review* **60** (1941).
- [45] L. Pitaevskii and S. Stringari, *Bose-Einstein condensation and superfluidity*, Vol. 164 (Oxford University Press, 2016).
- [46] S. Ostermann, F. Piazza, and H. Ritsch, Spontaneous Crystallization of Light and Ultracold Atoms, *Phys. Rev. X* **6** (2016).
- [47] W. J. Firth, I. Krešić, G. Labeyrie, A. Camara, and T. Ackemann, Thick-medium model of transverse pattern formation in optically excited cold two-level atoms with a feedback mirror, *Physical Review A* **96** (2017).
- [48] S. Ostermann, F. Piazza, and H. Ritsch, Probing and characterizing the growth of a crystal of ultracold bosons and light, *New Journal of Physics* **19** (2017).
- [49] I. Dimitrova, W. Lunden, J. Amato-Grill, N. Jepsen, Y. Yu, M. Messer, T. Rigaldo, G. Puentes, D. Weld, and W. Ketterle, Observation of two-beam collective scattering phenomena in a Bose-Einstein condensate, *Phys. Rev. A* **96** (2017).
- [50] T. Keller, V. Torggler, S. B. Jäger, S. Schütz, H. Ritsch, and G. Morigi, Quenches across the self-organization transition in multimode cavities, *New Journal of Physics* **20**, 025004 (2018).
- [51] Y. Guo, R. M. Kroeze, V. D. Vaidya, J. Keeling, and B. L. Lev, Sign-Changing Photon-Mediated Atom Interactions in Multimode Cavity Quantum Electrodynamics, *Physical Review Letters* **122** (2019).
- [52] Y. Guo, V. D. Vaidya, R. M. Kroeze, R. A. Lunney, B. L. Lev, and J. Keeling, Emergent and broken symmetries of atomic self-organization arising from Gouy phase shifts in multimode cavity QED, *Physical Review A* **99** (2019).
- [53] A. Glaetzle, M. Dalmonte, R. Nath, I. Rouschatzakis, R. Moessner, and P. Zoller, Quantum Spin-Ice and Dimer Models with Rydberg Atoms, *Physical Review X* **4** (2014).
- [54] A. W. Glaetzle, M. Dalmonte, R. Nath, C. Gross, I. Bloch, and P. Zoller, Designing Frustrated Quantum Magnets with Laser-Dressed Rydberg Atoms, *Physical*

- [Review Letters](#) **114** (2015).
- [55] M. Boninsegni, N. Prokof'ev, and B. Svistunov, Worm Algorithm for Continuous-Space Path Integral Monte Carlo Simulations, [Physical Review Letters](#) **96** (2006).
 - [56] M. Boninsegni, N. V. Prokof'ev, and B. V. Svistunov, Worm algorithm and diagrammatic Monte Carlo: A new approach to continuous-space path integral Monte Carlo simulations, [Physical Review E](#) **74** (2006).
 - [57] R. Lin, L. Papariello, P. Mognini, R. Chitra, and A. U. J. Lode, Superfluid–Mott-insulator transition of ultracold superradiant bosons in a cavity, [Physical Review A](#) **100** (2019).
 - [58] R. Lin, C. Georges, J. Klinder, P. Mognini, M. Büttner, A. U. J. Lode, R. Chitra, A. Hemmerich, and H. Keßler, Mott transition in a cavity-boson system: A quantitative comparison between theory and experiment, [SciPost Phys.](#) **11**, 30 (2021).
 - [59] S. Krämer, D. Plankensteiner, L. Ostermann, and H. Ritsch, QuantumOptics.jl: A Julia framework for simulating open quantum systems, [Comput. Phys. Commun.](#) **227** (2018).
 - [60] C. Maschler, I. B. Mekhov, and H. Ritsch, Ultracold atoms in optical lattices generated by quantized light fields, [The European Physical Journal D](#) **46** (2008).
 - [61] F. Brennecke, R. Mottl, K. Baumann, R. Landig, T. Donner, and T. Esslinger, Real-time observation of fluctuations at the driven-dissipative Dicke phase transition, [Proceedings of the National Academy of Sciences](#) **110** (2013).